Inorganic Chemistry

Article

pubs.acs.org/IC

Enhancement of the Luminescent Properties of a New Red-Emitting Phosphor, $Mn_2(HPO_3)F_2$, by Zn Substitution

Joseba Orive,[†] José L. Mesa,[‡] Rolindes Balda,[§,∥] Joaquín Fernández,[§,∥] Jesús Rodríguez Fernández,[⊥] Teófilo Rojo,[‡] and María I. Arriortua*[,†]

[†]Departamento de Mineralogía y Petrología, Facultad de Ciencia y Tecnología, Universidad del País Vasco, UPV/EHU, Apdo.644, E-48080 Bilbao, Spain

[‡]Departamento de Química Inorgánica, Facultad de Ciencia y Tecnología, Universidad del País Vasco, UPV/EHU, Apdo.644, E-48080 Bilbao, Spain

[§]Departamento Física Aplicada I, Escuela Técnica Superior de Ingeniería, Universidad del País Vasco, UPV/EHU, Alda. Urquijo s/n 48013 Bilbao, Spain

[∥]Centro de Física de Materiales CSIC-UPV/EHU and Donostia International Physics Center, Apdo. 1072, 20080 San Sebastián, Spain

[⊥]CITIMAC, Facultad de Ciencias, Universidad de Cantabria, 39005 Santander, Spain

Supporting Information

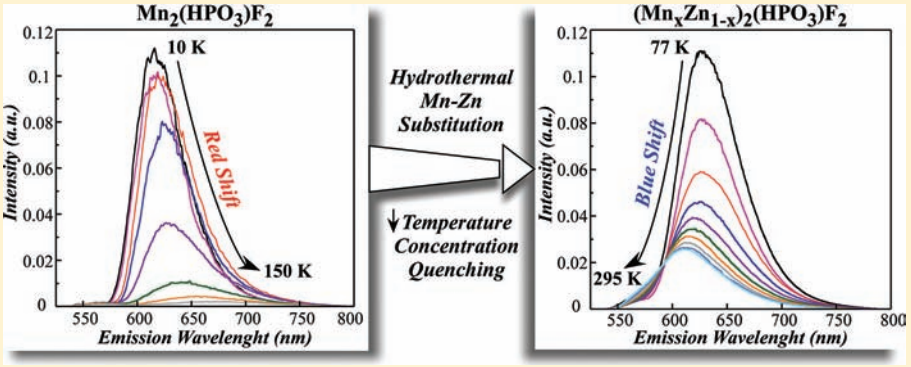

ABSTRACT: The $Mn_2(HPO_3)F_2$ phase has been synthesized as single crystals by using mild hydrothermal conditions. The compound crystallizes in the orthorhombic *Pnma* space group, with unit cell parameters of a = 7.5607(8), b = 10.2342(7), and c = 5.5156(4) Å, with Z = 4. The crystal structure consists of a three-dimensional framework formed by alternating (010) layers of $[MnO_3F_3]$ octahedra linked up by three connected $[HPO_3]$ tetrahedra. Luminescence measurements were performed at different temperatures between 10 and 150 K. The 10 K emission spectrum of the octahedrally coordinated Mn(II) cation exhibits a broad band centered at around 615 nm corresponding to the $^4T_1 \rightarrow {}^6A_1$ transition. In order to explore the effect of the Mn(II) concentration and the possibility of enhancing the luminescence properties of the Mn(II) cation in $Mn_2(HPO_3)F_2$, different intermediate composition members of the finite solid solution with the general formula $(Mn_xZn_{1-x})_2(HPO_3)F_2$ were prepared and their luminescent properties studied. The magnetic and specific heat behavior of $M_2(HPO_3)F_2$ (M = Mn, Fe) have also been investigated. The compounds exhibit a global antiferromagnetic ordering with a spin canting phenomenon detected at approximately 30 K. The specific heat measurements show sharp λ-type peaks at 29.7 and 33.5 K for manganese and iron compounds, respectively. The total magnetic entropy is consistent with spin S = 5/2 and S = 2 of Mn(II) and Fe(II) cations.

1. INTRODUCTION

The development of white-light-emitting diodes (WLEDs) is believed to be leading the way in new solid state lighting device generation due to the advantages of high brightness, small volume, energy savings, long durability, and environmental benefits in a number of applications.[1] Moreover, remarkable progress in the performance of LEDs with emissions in the near-ultraviolet wavelength range, 350−420 nm, has increased the research interest in materials which can be efficiently excited in this band. The widely used WLED devices on the market combine a blue LED with a yellow emission from the classical YAG/Ce phosphor.[2] The obtained light, used in, for example, traffic lights or outdoor lighting, looks bluish-cold, hence the need to incorporate a red-emitting phosphor to obtain warmer light for more sophisticated applications. Furthermore, red phosphors play a very important role for optimizing the color rendering index (CRI) of a white light

Received: June 8, 2011
Published: November 15, 2011

   dx.doi.org/10.1021/ic201226t | Inorg. Chem. 2011, 50, 12463−12476

source, which indicates the accuracy with which the light source renders the color of an objet.

The presently used red phosphors for WLEDs based on a near-UV chip are sulfide-based materials, such as $Y_2O_2S:Eu^{3+}$. However, as a result of their instability, which shortens the lifetime of WLEDs, there is an incessant search for chemically stable red phosphors.[3,4]

Phosphors based on inorganic phosphates generally have excellent thermal stability and stabilization of the ionic charge in the lattice.[5,6] Among them, the fluoroapatites (FAPs) family doped with rare earth or transition metal ions such as $Ca_5(PO_4)_3X:Sb^{3+}$, Mn^{2+}, and many metal-doped FAPs have been investigated in relation to their interesting spectroscopic properties.[7−11] In fact, it has been proved that FAPs present a good host lattice for luminescence and laser materials.[12−14] Considering covalency and anion polarizability arguments in the development of LED phosphors alone, fluoride and oxyfluoride hosts would normally be excluded due to the ionic nature of metal−F^- bonds, limiting compositional spaces when screening for new phosphor compositions. However, the study of unconventional systems, such as those based on the Sr_3AlO_4F structure doped with rare earths, sometimes leads to desirable properties far from typical expectations.[15−19]

In the search for new inorganic phases as novel hosts in phosphor materials, the replacement of the classical phosphate PO_4^{3-} units by the pseudopyramidal phosphite units HPO_3^{2-} can give rise to new structures due to the high versatility of the phosphite group for displaying properties of both tetrahedral and triangular oxoanionic groups.[20−22] In addition, the incorporation of the F^- anion in the inorganic framework of these compounds, following the synthetic route opened by Kessler et al.,[23] makes possible the synthesis of original and not structurally related phases to those found in literature.

Divalent manganese ions can be utilized to activate inorganic phosphors emitting in the red range of the spectrum. The ion electronic configuration is d^5, and the emission generally involves the $^4T_1(G)\rightarrow{}^6A_1(S)$ transition. However, due to the strong dependence of the emitting level on the crystal field strength of the crystal lattice site,[24] the peak of the Mn^{2+} emission band may lie in a broad spectral range from green to red depending on the specific characteristics of the crystal field (type of ligand coordination, covalency, etc).[25] In fact, this property makes Mn^{2+} center highly versatile and able to be used for tuning the spectral position of the emission band to a desirable position.

We have synthesized the $Mn_2(HPO_3)F_2$ compound, which has only one six-coordinated Mn^{2+} site. This feature allows the compound to act as a red-emitting phosphor when being excited at the UV−vis wavelength window. In order to improve the luminescent properties of the phase, we have partially replaced the Mn^{2+} ion (ionic radius 0.80 Å) with the Zn^{2+} ion (ionic radius 0.74 Å), giving rise to different intermediate composition members of the finite solid solution $(Mn_xZn_{1-x})_2(HPO_3)F_2$, present in the samples MnZn1, MnZn2, and MnZn3, keeping the crystalline structure of the stoichiometric compound as follows:

$$Mn_2(HPO_3)F_2,\ 1.875 \times 10^{22}\ \text{ions}\ Mn^{++}/cm^3 \quad (1)$$

$$MnZn1,\ \sim 1.10 \times 10^{22}\ \text{ions}\ Mn^{++}/cm^3 \quad (2)$$

$$MnZn2,\ \sim 0.68 \times 10^{22}\ \text{ions}\ Mn^{++}/cm^3 \quad (3)$$

$$MnZn3,\ \sim 0.45 \times 10^{22}\ \text{ions}\ Mn^{++}/cm^3 \quad (4)$$

The Zn^{2+} cation avoids the nonradiative transitions caused by the high concentration of manganese atoms. In addition, the Zn^{2+} cation enables the radiative emissions of manganese, thus improving the luminic efficiency of the manganese pure phase.

In the present work, we study the luminescent properties of the new manganese inorganic fluoro-phosphite $Mn_2(HPO_3)F_2$ together with the three nonstoichiometric samples (MnZn1, MnZn2, and MnZn3), of the $(Mn_xZn_{1-x})_2(HPO_3)F_2$ formula, obtained by substituting Mn^{2+} with Zn^{2+}. Moreover, we present the hydrothermal synthesis; crystal structure determination; and the thermal, spectroscopic, and magnetic behavior of the new manganese phase, $Mn_2(HPO_3)F_2$. The previously known iron phosphite $Fe_2(HPO_3)F_2$[26] was also studied in detail, emphasizing the magnetic study.

2. EXPERIMENTAL SECTION

2.1. Synthesis and Characterization. $[M_2(HPO_3)F_2]$ [M^{II} = Mn (**1**) and Fe (**2**)] were synthesized under mild hydrothermal conditions and autogenous pressure. H_3PO_3 (7.50 mmol for **1** and **2**), $MnCl_2{\cdot}4H_2O$ (2.25 mmol), and $Fe_2(SO_4)_3{\cdot}5H_2O$ (0.75 mmol) were dissolved in distilled water (30 mL). Then, 1.0 mL (27.8 mmol) of HF was added to the resulting solutions, and finally the pH was increased in all cases to approximately 4, using 2-methyl-piperazine. These reaction mixtures were sealed in PTFE-lined stainless steel pressure vessels. After 5 days at 170 °C, the vessels were slowly cooled to room temperature. A pink polycrystalline product for the manganese phase and colorless single crystals for the iron one were obtained, and then they were isolated by filtration, washed with water and acetone, and dried over P_2O_5 for 1 h. In order to obtain single crystals of **1**, for the X-ray diffraction study (Figure S1, Supporting Information), we added 2.25 mmol of $CeCl_3{\cdot}7H_2O$, to the synthesis described above, which seems to act, only, as a sort of mineralizer in the reaction.

Although amine was used as the trial template, no organic species were detected by elemental analyses. But the 2-methylpiperazine molecule not only acts as a pH modifier but also plays a structure-directing role[27] in the formation of the compounds, because we tried to use NaOH instead of the organic additive with no success.

Compound **2** was previously synthesized by Liu et al.,[26] in the $FeCl_2{\cdot}2H_2O-H_3PO_3-$imidazole$-HF-H_2O$ reaction system with a molar ratio of 1:3:4:4:280 at 160 °C for 7 days.

Samples MnZn1, MnZn2, and MnZn3 were synthesized by using the synthesis methodology proposed in order to obtain the pure manganese phase as a polycrystalline product and the following 1.125:1.125, 0.45:1.8, and 0.225:2.025 $MnCl_2{\cdot}4H_2O/ZnCl_2$ molar ratios, respectively. The existence of Zn in the samples was confirmed by FRX. In this case, the addition of $CeCl_3{\cdot}7H_2O$ had no effect on the synthesis, and fine grained powders were obtained in all cases.

The compositions of the products were calculated with the aid of ICP-AES spectroscopy. The amount of the fluoride anion was calculated by using a selective electrode. $[Mn_2(HPO_3)F_2]$ (**1**), Calcd: Mn, 48.2; F, 16.7. Found: Mn, 48.0(1); F, 16.4(1). $[Fe_2(HPO_3)F_2]$ (**2**), Calcd: Fe, 48.7; F, 16.5. Found: Fe, 48.5(2); F, 16.2(1). The densities measured by pycnometry are 3.51(2) and 3.71(2) g cm^{-3} for **1** and **2**, respectively.

2.2. Single Crystal X-Ray Diffraction Study. A tabular single crystal with dimensions 0.134 × 0.072 × 0.014 mm of **1** was selected under a polarizing microscope and mounted on a glass fiber. Single-crystal X-ray diffraction data were collected at 100 K from a STOE IPDS automated diffractometer (Mo Kα radiation) equipped with a CCD detector. The Lorentz polarization and absorption corrections were made with the diffractometer software, taking into account the size and shape of the crystal. The crystal structure of **1** was solved by direct methods, using the SHELXS 97 computer program,[28] and refined by full matrix least-squares based on F^2, using SHELXL 97[29] in

dx.doi.org/10.1021/ic201226t | Inorg. Chem. 2011, 50, 12463−12476

the centrosymmetric *Pnma* orthorhombic space group. The Mn(II) cation occupies a general position, and the P occupies a special position. There are two positions, a general one and a special one, for the O atoms. The F atom was differed from the O atoms on the basis of the nonexistence of bonds with P atoms and the slightly lower thermal parameters. All non-hydrogen atoms were refined anisotropically.

All structure drawings were made using the ATOMS program.[30] The crystallographic data of phase **1** are given in Table 1. The selected bond distances and angles are reported in Table 2.

Table 1. Crystallographic Data and Structure Refinement Parameters for 1, Obtained by Single Crystal X-Ray Diffraction

sample	compound **1**
formula	$Mn_2(HPO_3)F_2$
mw (g mol^{-1})	227.86
crystal system	orthorhombic
space group (no. 62)	*Pnma*
a, Å	7.5607(8)
b, Å	10.2342(7)
c, Å	5.5156(4)
V, Å^3	426.78(6)
Z	4
ρ_{calc}, g cm^{-3}	3.546
crystal size (mm)	0.134 × 0.072 × 0.014
F(000)	432
temperature, K	100
diffractometer	STOE IPDS 2T
μ (mm^{-1})	6.234
radiation, λ(Mo Kα), Å	0.71073
limiting indices *h*, *k*, *l*	$h \pm 10$, $k \pm 14$, $l \pm 7$
θ range (deg)	3.98−29.59
no. reflns (indep.)	600
no. reflns (obsd.)	476
R(int)/R(σ)[a]	0.0511/0.0239
R [I > 2σ(I)][a]	R1 = 0.019, wR2 = 0.040
R [all data][a]	R1 = 0.030, wR2 = 0.042
GOF	0.927
max. and min. e density (e Å^{-3})	0.355, −0.612

[a]R1 = $[(|F_o| - |F_c|)]/|F_o|$. wR2 = $[[w(|F_o|^2 - |F_c|^2)^2]/[w(|F_o|^2)^2]]^{1/2}$; $w = 1/[\sigma^2|F_o|^2 + (xp)^2 + yp]$, where $p = [|F_o|^2 + 2|F_c|^2]/3$; $x = 0.0272$, $y = 0.0000$ for **1**.

2.3. Powder X-Ray Diffraction Study. X-ray powder diffractions for qualitative and quantitative phase analysis using the Rietveld method with the FULLPROF program[31] for the samples MnZn1, MnZn2, and MnZn3 and for $Fe_2(HPO_3)F_2$ (**2**) were recorded using a Bruker D8 Advance Vario powder diffractometer equipped with a Cu tube, Ge(111) incident beam monochromator (Cu Kα1 = 1.5406 Å), and a Sol-X energy dispersive detector. The samples were mounted on a zero background silicon wafer embedded in a generic sample holder. Data were collected from 15 to 100° 2θ (step size = 0.02° and time per step = 30 s) at room temperature. Fixed divergence and an antiscattering slit giving a constant volume of sample illumination were used.

2.4. Physicochemical Characterization Techniques. Thermogravimetric analyses for **1** and **2** were performed on an SDC 2960 simultaneous DSC-TGA TA Instruments machine. Crucibles containing 20 mg of every sample were heated at a rate of 10 °C/min from room temperature to 800 °C. Temperature dependence X-ray diffraction experiments for **1**, **2**, and the sample MnZn3 were carried out in the air with a Bruker D8 Advance diffractometer (Cu Kα radiation) equipped with a variable-temperature stage (HTK2000), a Pt sample heater, and a Vantec high-speed one-dimensional detector with 6° of angular aperture. The powder patterns were recorded in the $8 \leq 2\theta \leq 38°$ range (step size = 0.033° and time per step = 0.4 s) at intervals of 15 °C, increasing the temperature at 10 °C min^{-1} from room temperature to 795 °C. The IR spectra (KBr pellets) were obtained with a JASCO FT/IR-6100 spectrophotometer in the 400−4000 cm^{-1} range. Diffuse reflectance spectra were registered at room temperature on a Cary 600i for **1** and on a Cary 5000 spectrometer for **2** in the 210−2000 nm range. Magnetic measurements on the powdered sample were performed in the temperature range 5.0−300 K for **1** and **2**, at 0.1, 0.05, and 0.01 T using a Quantum Design MPMS-7 SQUID magnetometer. This value is in the range of linear dependence of magnetization versus magnetic field even at 5.0 K. The emission measurements for **1** and the samples MnZn1, MnZn2, and MnZn3 were made using the 514 nm line of an argon laser as an exciting light. The fluorescence was analyzed with a 0.25 m monochromator, and the signal was detected by a Hamamatsu R636 photomultiplier. For the fluorescence dynamic measurements, a digital oscilloscope was used to record the decay signals. The samples temperature was varied between 10 and 295 K with a continuous flow cryostat. Heat capacity measurements for **1** and **2** were carried out using the two-τ relaxation method, using a PPMS system, with magnetic fields up to 9 T and temperatures down to 2 K.

3. RESULTS AND DISCUSSION

3.1. Structure Description. The crystal structure of compound **1** consists of a three-dimensional network formed by alternating (010) layers of $[MnO_3F_3]$ octahedra (*A* and *B*)

Table 2. Bond Distances (Å) and Angles (deg) for 1[a]

Octahedron $[Mn(1)O_3F_3]$						
Mn(1)	F(1)	F(1)^{v}	O(1)^{i}	F(1)^{vi}	O(2)	O(1)
O(1)	81.41(5)	89.03(5)	78.95(6)	90.33(5)	170.74(7)	***2.224(1)***
O(2)	89.58(6)	94.59(6)	100.17(6)	98.81(6)	***2.185(1)***	
F(1)^{vi}	170.79(6)	76.18(5)	85.31(5)	***2.156(1)***		
O(1)^{i}	97.00(5)	157.88(5)	***2.149(1)***			
F(1)^{v}	99.50(3)	***2.134(1)***				
F(1)	***2.114(1)***					
Tetrahedron $[HP(1)O_3]$						
P(1)	O(1)		O(1)^{vii}	O(2)^{ii}		H(1)
H(1)	108(1)		108(1)	107(2)		***1.25(3)***
O(2)^{ii}	111.24(7)		111.24(7)	***1.554(2)***		
O(1)^{vii}	111.2(1)		***1.532(1)***			
O(1)	***1.532(1)***					

[a]Symmetry codes: i = $-x, -y + 1, -z$. ii = $-x + 1/2, -y + 1, z - 1/2$. iii = $x + 1/2, y, -z + 1/2$. iv = $x, -y + 1/2, z$. v = $-x + 1/2, -y + 1, z + 1/2$. vi = $x - 1/2, y, -z + 1/2$. vii = $x, -y + 3/2, z$.

dx.doi.org/10.1021/ic201226t | *Inorg. Chem.* 2011, 50, 12463−12476

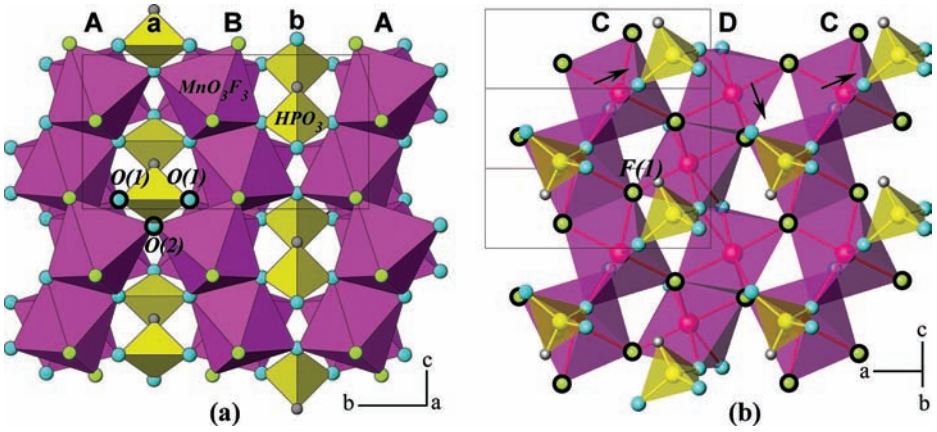

Figure 1. (a) Polyhedral view of the crystal structure of $Mn_2(HPO_3)F_2$ along the [100] direction. (b) Connectivity between the octahedra layers and the tetrahedra units.

linked between them through the three-connected $[HPO_3]$ tetrahedra (*a* and *b*; Figure 1a). The octahedra share the O(1)−O(1) and F(1)−F(1) edges giving rise to zigzag chains, parallel to the [001] direction. The chains are linked by the F(1) fluorine atoms to construct the layers (Figure 1b). The connectivity between the octahedra and the tetrahedra layers is shown by arrows that point at the linkage direction existing in the *C* and *D* adjacent chains. The *A* and *B* octahedra layers are related through *m* symmetry mirrors; however, the $[HPO_3]$ units are related via inversion centers and translational symmetry elements characteristic of the *Pnma* space group (Figure S2, Supporting Information). The geometrical arrangement of the oxygen and fluorine atoms in the $[MnO_3F_3]$ octahedra gives rise to approximately perpendicular planes (see inset Figure 3).

In the crystal structure of $Fe_2(HPO3)F_2$, Liu et al.[26] described the $[FeO_3F_3]$ octahedra chains like a result of an infinite −Fe−F−Fe−O−Fe− linkage along the *c* axis. They also observed the existence of −Fe−F−Fe− layers when all of the O atoms are omitted.

In the $[MnO_3F_3]$ octahedra, the M−O bond distances are 2.149(1) and 2.224(1) Å for O(1). The M−O(2) bond length is 2.185(1) Å. The M−F bond lengths are 2.114(1), 2.156(1), and 2.134(1) Å. The values of the *cis* and *trans* angles in these octahedra are the ones habitually found for the slightly distorted octahedral coordination. The octahedra suffer the main distortion in the $F(1)^{v}$−Mn(1)−$O(1)^{i}$ *trans* angle, which presents a minimum value of 157.88(5)°. The distortion of the $[MnO_3F_3]$ octahedron, calculated with the Álvarez et al. method[32] using the SHAPE v1.1a program,[33] is $S(O_h)$ = 1.380, near the value for the octahedral ideal symmetry (S(Oh) = 0.00).

In the $[HPO_3]$ tetrahedra, the P−O bond distances are 1.532(1) and 1.554(2) Å for O(1) and O(2), respectively. The bond angles of these oxoanions are near to the ideal value of 109°, as is expected for an sp^3 hybridization of the phosphorus atom. The distortion of the $[HPO_3]$ polyhedra from the tetrahedral symmetry has a mean value of $S(T_d)$ = 0.780, indicating a symmetry near to the ideal one ($S(T_d)$ = 0.00)).[34]

3.2. Rietveld Refinements. For MnZn1, MnZn2, and MnZn3, the unit cell parameters and the atomic coordinates of **1** were used as a starting point of the Rietveld refinement. Taking into account the ionic radius similarity between Mn^{2+} (0.80 Å) and Zn^{2+} (0.74 Å) in an octahedral environment, the same atomic position was considered for two cations. In this way, it was possible to refine the occupation factors of the manganese and zinc atoms.

After a preliminary Rietveld refinement of the three samples, the existence of minority phases with similar unit cell parameters to those of the majority solid solutions was observed. So, a second phase, with the same initial structural model as the main phase, was added to each sample. The multiphase Rietveld analyses were carried out in two general steps. First, the profile and structural model of the majority phases (-F1 suffix) were cycled. In a second step, the profile and structural model of the minority phases (-F2 suffix) were cycled, fixing the profile and structural parameters of the majority phases.

In the profile refinements of the phases (-F1 and -F2), the systematic 2θ shift; peak shape (pseudo-Voigt); *U*, *V*, and *W* half-width parameters for the profile function; the previously obtained unit cell parameters; asymmetry parameters; and the background were refined.

For the structural model refinements, first the occupancy factors of Mn(1) and Zn(1) as interdependent variables and then the atomic coordinates and the atomic displacement (thermal) parameters of all atoms were refined. Three different isotropic displacement parameters were refined: one for the manganese and zinc atoms; a second for the phosphorus atoms; and a final one for the oxygen, fluorine, and hydrogen atoms. The atomic positions and thermal parameters of the Mn(1) and Zn(1) atoms were restrained to be equal. So the dependence of the thermal value on the population factor for the Mn(1) and Zn(1) atoms is also equal. Some soft constraints were included to have chemically correct structural models. For the P(1)−H(1) bond distance, we have soft constrained to 1.30(5) Å for the MnZn1-F1 phase and 1.30(2) Å for the MnZn1-F2, MnZn3-F1, and MnZn3-F2 phases. For this last phase, it was also necessary to include P(1)−O(2) and Mn(1)−O(1) soft constraints of 1.55(1) Å and 2.10(3) Å, respectively. In the case of the MnZn2 and MnZn3 samples, it was necessary to refine the preferred-orientation parameters of the 020 reflections.

Finally, all parameters (profile and structural) were refined simultaneously to obtain correct estimated standard deviations, obtaining a good agreement between the experimental and calculated diffractograms in the three samples (Figure 2). This good fit has permitted the refinement of the occupation factors of the manganese and zinc atoms, and the calculation of the weight percentage, for each two phases of each sample by modifying the ATZ parameter (Table 3). (See Tables S1−S12,

dx.doi.org/10.1021/ic201226t | *Inorg. Chem.* 2011, 50, 12463−12476

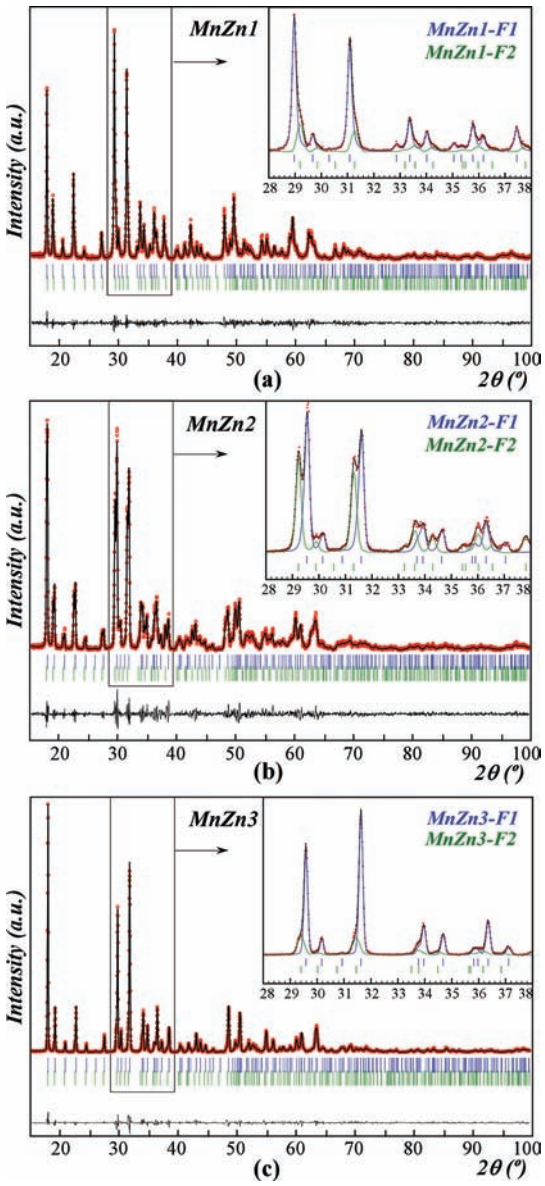

Figure 2. Observed, calculated, and difference X-ray powder diffraction patterns for the samples (a) MnZn1, (b) MnZn2, and (c) MnZn3 with the initial structural model of $Mn_2(HPO_3)F_2$ (**1**).

Supporting Information, for atomic coordinates and bond distances and angles of the phases present in the MnZn1, MnZn2, and MnZn3 samples.)

The evolution of the parameters and the volume of the unit cell with the manganese occupation factor is plotted for the majority phases, MnZn1-F1 (~81.2%) and MnZn3-F1 (~80.2%) and MnZn2-F1 (~58.1%) and MnZn2-F2 (~41.9%) (Figure S3a, Supporting Information). An approximately linear decrease of the unit cell parameters and volume with the decrease of manganese or increase of zinc in the metal position is observed. These data are in good agreement with the ionic radius of both cations, Mn^{2+} (0.80 Å) and Zn^{2+} (0.74 Å), and consistent with Vegard's law[35] (Figure S3a, Supporting Information). Similar behavior is observed when the M−O and M−F distances are represented with respect to the occupation factor of manganese in each phase (Figure S3b, Supporting Information).

However, in relation to minority phases, MnZn1-F2 (~18.8%) and MnZn3-F2 (~19.8%), probably the deviations from their occupation factors as well as cell parameters are overestimated due to their low weight percentage.

It was also observed that in the phases with more quantity of zinc than of manganese, as in MnZn3-F1 and MnZn2-F1 (85 and 70% Zn in the Mn site, respectively), the octahedra suffer a rearrangement of the oxygen and fluorine atoms giving rise to a different distribution of (Mn,Zn)−O and (Mn,Zn)−F distances. In particular, the shortening suffered by the (Mn,Zn)−$O(1)^{v}$ and (Mn,Zn)−$F(1)^{iv}$ distances is noteworthy, whose directions are more or less parallel to the *c* axis (Figure 3).

In spite of the variation of the bond distances, the distortion values of the $[(Mn,Zn)O_3F_3]$ and $[HPO_3]$ polyhedra for the $(Mn_xZn_{1-x})_2(HPO3)F_2$ finite solid solutions calculated with the SHAPE v1.1a program[33] are similar to those presented by the manganese pure phase, **1** (see Table S13 and Figure S4, Supporting Information).

For the Rietveld refinement of phase **2**, the structural model of **1**, changing Mn(1) for Fe(1) atom, was also used. Finally, good agreement between the experimental and calculated diffractograms was obtained (Figure S5 and Table S14, Supporting Information). So, the proposed chemical formula for **2** is $Fe_2(HPO_3)F_2$, confirming the isostructurality between the **1** and **2** compounds and the purity phase of **2** to the posterior characterization. (See Tables S15 and S16, Supporting Information, for atomic coordinates and bond distances and angles of the Rietveld refinement of **2**.)

3.3. Thermal Study. The thermogravimetric curves of the two phases show an initial mass loss of approximately 3% and 1% until 420 °C, for **1** and **2**, respectively, which is attributed to the elimination of the water adsorbed by the compounds. After this process, the elimination of the fluoride anions in the 420−570 °C and 420−525 °C ranges for **1** and **2**, respectively, takes place. Around 520 and 580 °C, a mass increase in the thermogravimetric curves of **1** and **2**, respectively, is observed, probably due to the oxidation from phosphite to phosphate. After this oxidation process, in the 630−800 °C range, the formation of the inorganic residue for phase **1** occurs, which is formed by $Mn_3(PO_4)_2$ [S.G. $P2_1/c$, a = 8.948(2) Å, b = 10.050(2) Å, c = 24.084(2) Å, β = 120.5°].[36] For phase **2**, the inorganic residues appear in the 630−800 °C range and are constituted by a mixture of $Fe(PO_4)$ [S.G. $P3_12_1$, a = 5.019(1) Å, c = 11.226(2) Å, γ = 120°],[37] $Fe_3(PO_7)$ [S.G. $R3m$, a = 8.006(5) Å, c = 6.863(5) Å, γ = 120°],[38] and Fe_2O_3 [S.G. $R\bar{3}c$ a = 5.0355(5) Å, c = 13.7471(7) Å, γ = 120°][39] (Figure S6, Supporting Information).

The thermal behavior of compounds **1** and **2** and the sample with the greater amount of zinc, MnZn3, was also studied by using time-resolved X-ray thermodiffractometry in the air. The thermodiffractograms remain unchanged until 420 °C for **1** (Figure S7a, Supporting Information) and **2** (Figure S8, Supporting Information), which indicates that this temperature is the limit of thermal stability of the phases. In turn, in Figure S7b (Supporting Information), it may be seen that the thermodiffractogram of sample MnZn3, which is much more crystalline than $Mn_2(HPO_3)F_2$ (**1**), remains unchanged until 450 °C. So, it seems that the insertion of Zn into the crystal structure of the pure manganese phase **1** improves the crystallinity and the thermal stability of the resulting structure in the sample MnZn3. For **1**, at around 435 °C, the crystallization of Mn_2O_3 [S.G. $I2_13$, a = 9.41 Å][40] starts. At 555 °C, the MnO [S.G. $Fm\bar{3}m$, a = 4.446(1) Å][41] crystallizes, and finally, from 660 to 795 °C, the $Mn_3(PO_4)_2$ that was detected in the

dx.doi.org/10.1021/ic201226t | Inorg. Chem. 2011, 50, 12463–12476

Table 3. Crystallographic Data and Structure Rietveld Refinement Parameters for the MnZn1, MnZn2, and MnZn3 Samples

sample	MnZn1		MnZn2		MnZn3	
phase	MnZn1-F1	MnZn1-F2	MnZn2-F1	MnZn2-F2	MnZn3-F1	MnZn3-F2
formula	$Mn_{1.26}Zn_{0.74}(HPO_3)F_2$	$Mn_{0.6}Zn_{1.4}(HPO_3)F_2$	$Mn_{0.6}Zn_{1.4}(HPO_3)F_2$	$Mn_{0.78}Zn_{1.22}(HPO_3)F_2$	$Mn_{0.3}Zn_{1.7}(HPO_3)F_2$	$MnZn(HPO_3)F_2$
M.O.F.[a]	Mn:0.63(4)	Mn:0.29(5)	Mn:0.30(6)	Mn:0.39(7)	Mn:0.15(4)	Mn:0.50(9)
	Zn:0.37(4)	Zn:0.71(5)	Zn:0.70(6)	Zn:0.61(7)	Zn:0.85(4)	Zn:0.50(9)
M.W.[a]	235.587	242.485	242.485	240.604	238.304	245.621
ATZ	942.349	969.942	969.942	962.416	953.219	982.484
phase (%)	~81.2	~18.8	~58.1	~41.9	~80.2	~19.8
Mn/unit cell	5.04	2.4	2.4	3.12	1.2	4
ionic density (ions/cm^3)	1.220×10^{22}	0.593×10^{22}	0.613×10^{22}	0.774×10^{22}	0.308×10^{22}	1.008×10^{22}
	$\sim 1.10 \times 10^{22}$		$\sim 0.68 \times 10^{22}$		$\sim 0.45 \times 10^{22}$	
% Mn bulk	~57		~34		~22	
a, Å	7.4688(3)	7.420(1)	7.3443(4)	7.4112(5)	7.3350(2)	7.3748(9)
b, Å	10.1538(4)	10.109(1)	10.0276(4)	10.0955(5)	10.0195(1)	10.065(1)
c, Å	5.4459(2)	5.3883(8)	5.3149(3)	5.3883(4)	5.3049(1)	5.3447(7)
V, Å^3	413.00(3)	404.6(1)	391.41(3)	403.15(4)	389.87(1)	396.73(8)
Z	4	4	4	4	4	4
I.R.[a]	272	294	271	276	249	296
S.P.[a]	18	18	18	18	18	18
P.P.[a]	28	27	37	37	40	38
S.D.C.[a]	1	1	0	0	1	3
R_{Bragg}	2.30	2.71	2.71	2.74	2.97	7.03
R_f	1.84	2.41	2.19	2.28	3.54	4.63
R_p	11.3		12.3		11.2	
R_{wp}	15.4		16.1		14.5	
R_{exp}	14.75		11.99		10.43	
χ^2	*1.08*		*1.79*		*1.94*	

[a]M.O.F = metal occupation factor, M.W. = molecular weight (g mol^{-1}), I.R. = independent reflections, S.P. = structural parameters, P.P. = profile parameters, S.D.C. = soft distance constraints.

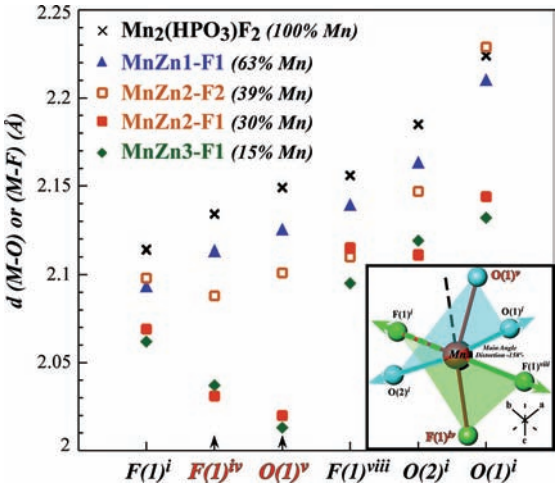

Figure 3. Distribution of the M−O and M−F bond distances in the $[MnO_3F_3]$ and $[(Mn,Zn)O_3F_3]$ octahedra belonging to $Mn_2(HPO_3)F_2$ (**1**) and to the main phases, MnZn1-F1, MnZn2-F2, MnZn2-F1, and MnZn3-F1. (Symmetry codes: i = *x*, *y*, *z*; ii = $x + 1/2, -y + 1/2, -z + 1/2$; iii = $-x, y + 1/2, -z$; iv = $-x + 1/2, -y, z + 1/2$; v = $-x, -y, -z$; vi = $-x + 1/2, y + 1/2, z + 1/2$; vii = $x, -y + 1/2, z$; viii = $x + 1/2, y, -z + 1/2$.)

thermogravimetric study crystallizes. For sample MnZn3, in the 465−645 °C temperature range, some maxima were observed that could not be identified. Finally, from 645 °C on, $Zn_3(PO_4)_2$ [$P2_1/n$ (14), a = 7.5490 Å, b = 8.4990 Å, c = 5.0491 Å, β = 95.03°][42] crystallizes. The characterization of the inorganic residues of **2** is made difficult by the fluorescence exhibited by the iron phases; however, it was possible to identify the existence of $Fe(PO_4)$,[37] $Fe_3(PO_7)$[38], and Fe_2O_3[39] at temperatures near 700 °C. These residues were also detected in the thermogravimetric experiment.

The thermal expansion coefficients for compounds **1** and **2** have been calculated from the data obtained by the thermodiffractometry, using the expression $V(T) = V_{Tr} \exp[\alpha_0(T - Tr)]$,[43] where V_{Tr} is the volume at the initial room temperature and α_0 is the thermal expansion coefficient. The results are shown in Table S17 (Supporting Information), and the plots with these results are given in Figure S9 (Supporting Information).

3.4. Infrared Spectroscopy. IR spectra of **1** and **2** and the MnZn1, MnZn2, and MnZn3 samples exhibit bands corresponding to the vibrations of the $(HPO_3)^{2-}$ phosphite oxoanions. In all of them, around 2500 cm^{-1}, a band corresponding to the stretching vibrational mode, ν(P−H), of the phosphite can be observed in the spectra. The presence of this band is in good agreement with the existence of one crystallographically independent phosphite anion in the structures of **1** and **2**.[44] At lower frequencies, approximately 1065, 1030, and 975 cm^{-1}, those bands corresponding to asymmetrical stretching $\nu_{as}(PO_3)$, deformation δ(PH), and symmetrical stretching $\nu_s(PO_3)$ modes of the $(HPO_3)^{2-}$ anion, respectively, appear. Finally, the symmetrical and antisymmetrical deformation vibrations, $\delta_s(PO_3)$ and $\delta_{as}(PO_3)$, are detected at approximately 600 and 530 cm^{-1}, respectively (Figure S10 and Table S18, Supporting Information). In the spectra of the MnZn1, MnZn2, and MnZn3 samples, the band

dx.doi.org/10.1021/ic201226t | Inorg. Chem. 2011, 50, 12463–12476

corresponding to the ν(P−H) mode broadens and shifts to high frequencies as the zinc content increases in the bulk of the samples. The broadening is due to the overlapping of the bands corresponding to the different ν(P−H) modes of the phosphite groups of the two finite solid solution members of each sample. It is thought that the wavelength shift may be a result of the pseudotetrahedra distortion caused by the progressive substitution of Mn^{2+} with Zn^{2+} ions in the MnZn1, MnZn2, and MnZn3 samples (Figure S11, Supporting Information).

3.5. UV−Vis and Luminiscent Spectroscopies. *3.5.a. Diffuse Reflectance Spectrum of the Stoichiometric Compound $Mn_2(HPO_3)F_2$.* The diffuse reflectance spectrum exhibits several weak spin-forbidden d−d bands, at approximately 340, 350, 400, 430, and 515 nm, similar to those of other octahedrally coordinated Mn^{2+} complexes which correspond to transitions from the $^6A_1(^6S)$ ground state to $^4E(^4D)$, $^4T_2(^4D)$, $^4E(^4G)$, $^4T_2(^4G)$, and $^4T_1(^4G)$ terms, respectively. The *Dq* and Racah parameters have been calculated by fitting the experimental frequencies obtained from the diffuse reflectance spectrum to an energy level diagram for an octahedral d^5 high-spin system.[45] The values obtained are Dq = 760, B = 680, and C = 3635 cm^{-1}, which are in the range habitually found for octahedrally coordinated Mn(II) compounds[25,45] but lower than those found for the free ion, indicating a noticeable degree of covalent interaction between Mn^{2+} and the surrounding ligand.[46]

It is worth noticing that the bandwidths of the spectral bands due to d−d transitions are proportional to the slope of the upper state relative to that of the ground state in the energy level−crystal field diagrams. Comparison of the spectrum in Figure 4 with the energy level diagram[24] of the d^5 system shows

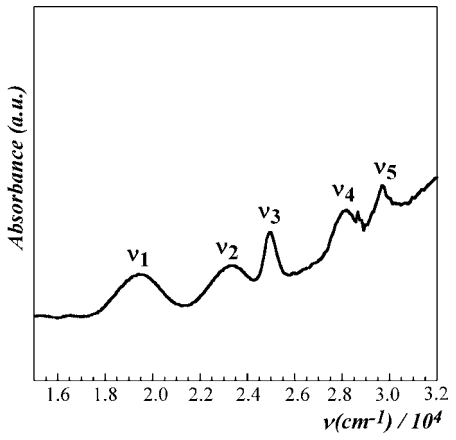

Figure 4. Diffuse reflectance spectrum of $Mn_2(HPO_3)F_2$.

that this expectation is fulfilled. Thus, in agreement with experimental results, the narrowest bands correspond to transitions $^6A_1(^6S)\rightarrow(^4E(^4D), ^4E(^4G))$, with zero slope (frequencies ν_3 and ν_5 in Figure 4).

3.5.b. $Mn_2(HPO_3)F_2$ Luminescence. In this compound, luminescence measurements have been carried out at different temperatures between 10 and 150 K under excitation in the $^6A_1\rightarrow{}^4T_1$ absorption band of Mn^{2+} using the 514 nm line of an Ar^+ laser.

Figure 5 displays the emission spectra of $Mn_2(HPO_3)F_2$ as a function of the temperature. According to the expected octahedral environment for the Mn^{2+} ions, the 10 K emission spectrum is characterized by a broad band centered at around

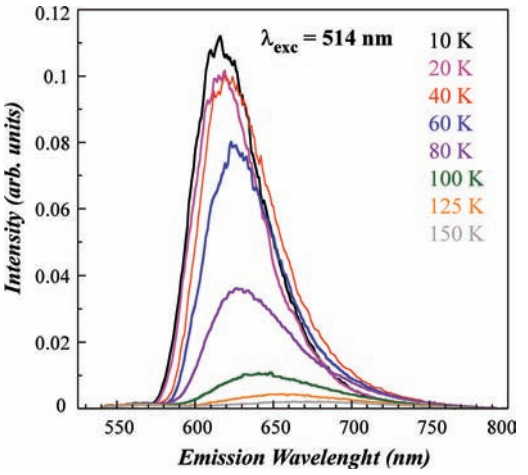

Figure 5. Emission spectra of $Mn_2(HPO_3)F_2$ as a function of the temperature.

615 nm corresponding to the $^4T_1\rightarrow{}^6A_1$ transition. As can be seen, as the temperature increases, there is a decrease of the emission intensity due to an enhancement of nonradiative processes. Moreover, the emission broadens and shifts to red as the temperature increases. The full width at half-maximum (fwhm) changes from 52 to 113 nm as the temperature rises from 10 K to 150 K. For temperatures higher than 150 K, the luminescence is practically quenched. The decrease of the emission intensity as well as the broadening of the emission band can be explained by the configurational coordinate diagram.[47] When the configurational coordinate curves of the excited and ground states intersect with each other, an electron in the excited state can cross the intersection assisted by thermal energy and reaches the ground state nonradiatively. This process can be described by a transition probability per unit time given by $w = s\ e^{-(\Delta E)/(k_B T)}$, where s is a frequency constant, ΔE is the activation energy, k_B is the Boltzmann constant, and T is the temperature.[25] As the temperature increases, the nonradiative transition probability by thermal activation increases, which quenches the luminescence. The enhancement of the electron−phonon interaction at high temperature, due to the increased population density of phonons, broadens the fwhm.[47,48]

Figure 6 shows the integrated emission intensities as a function of the temperature together with the fit to the Arrhenius equation

$$I(T) \approx \frac{I_0}{1 + s\ e^{-\Delta E/k_B T}}$$

where $I(T)$ is the intensity at a given temperature, I_0 is the low temperature initial intensity, s is a constant, k_B is the Boltzmann constant, T is the temperature, and ΔE is the activation energy. The best fit to the equation yields a value of 290 cm^{-1} for ΔE.

The decay kinetics of the $^4T_1\rightarrow{}^6A_1$ broad emission were obtained between 10 and 150 K under excitation at 514 nm by collecting the luminescence at the peak wavelength of the emission band. The lifetime values were obtained by fitting the experimental decays to a single exponential function.

As can be seen in Figure 7, the lifetimes are significantly reduced as the temperature increases from 10 to 150 K and follow a qualitative behavior similar to the one shown in Figure 6, for the integrated emission intensities, suggesting that lifetime decrease is due to thermal quenching. The lifetime of Mn^{2+} ion can be written as $\tau = (W_R + W_{NR})^{-1}$, where W_R and W_{NR} are the

dx.doi.org/10.1021/ic201226t | Inorg. Chem. 2011, 50, 12463–12476

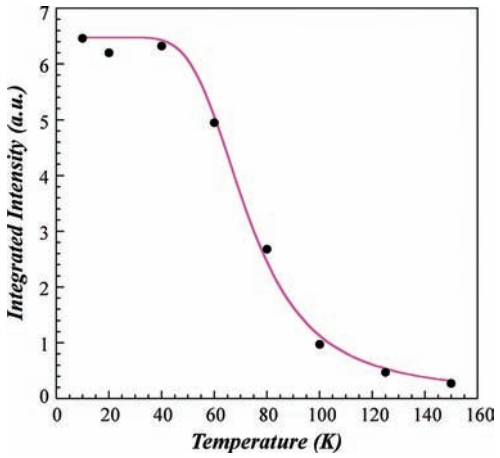

Figure 6. Integrated emission intensities (symbols) as a function of the temperature. The continuous line is the fit to eq 1.

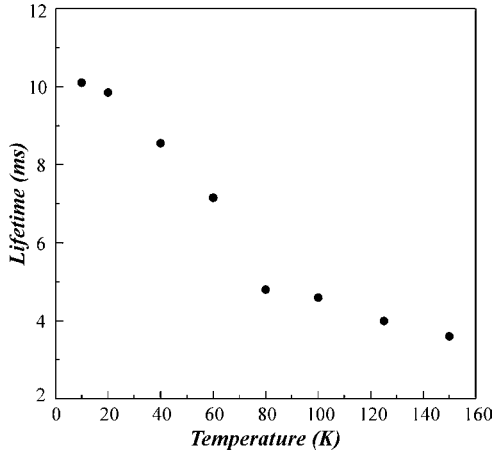

Figure 7. Lifetimes of $Mn_2(HPO_3)F_2$ as a function of the temperature.

radiative and nonradiative transition probabilities, respectively. As we have seen before, the probability that the manganese center will make a transition from the excited state to the ground state nonradiatively depends on the thermal activation energy ΔE necessary for the electron to cross the intersection point and reach the ground state. Therefore, W_{NR} will be given by $W_{NR} = s\ e^{-(\Delta E)/(k_B T)}$, and the lifetime can be expressed by

$$\frac{1}{\tau} = \frac{1}{\tau_R} + s \exp\left(-\frac{\Delta E}{k_B T}\right)$$

where $\tau_R = (W_R)^{-1}$ and s is a frequency factor.

Symbols in Figure 8 show the decay probability as a function of the temperature, and the continuous curve is the best fit to this equation. The fit gives a value of 130 cm^{-1} for the activation energy ΔE. However, this number is smaller than the one obtained for the thermal quenching of the integrated emission energy (290 cm^{-1}). This result could be related to the existence of some additional temperature dependent nonradiative energy transfer processes associated with the high ion concentration, which could be enhanced by phonon assistance.

3.5.c. $(Mn_xZn_{1-x})_2(HPO_3)F_2$ Luminescence. As we have already mentioned in the Introduction, the optical properties of manganese are very sensitive to the coordination number and to the strength of the ligand field of the matrices because 3d electrons are directly exposed to the surrounding environment

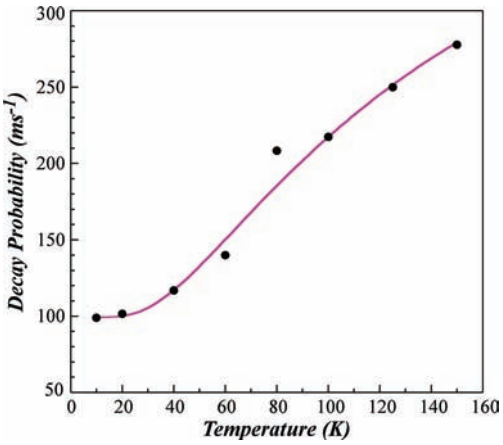

Figure 8. Decay probability as a function of the temperature (symbols) and fitting to eq 2.

and present, in general, a large electron−phonon coupling. From a practical point of view, these characteristics could help to tailor specific applications. For example, if we search for lighting applications, high emitting efficiencies and long emission lifetimes are welcome; however, for display applications, a long lifetime could produce an undesirable afterglow effect.

As we have seen above, the $Mn_2(HPO_3)F_2$ luminescence exhibits a strong temperature quenching which impedes practical applications. This situation, found in most of the concentrated systems, can be overcome by partially substituting the luminescent species by other ions having a similar ion size in order to keep the basic properties of the luminescent ion unchanged. For example, in the case of Mn^{2+}, an appropriate substitute is Zn^{2+}. This ion allows one to maintain the crystal structure of the compound as well as to enhance in some cases the luminescence of Mn^{2+} by energy transfer processes when pumping in the UV.

There are many examples in the literature of zinc-based hosts doped with increasing amounts of Mn^{2+}, for instance, the green-emitting phosphors, Zn_2SiO_4:Mn,[49] Zn_2GeO_4:Mn,[50] $ZnAl_2O_4$:Mn,[50] $Li_2ZnGe_3O_8$:Mn,[50] $ZnGa_2O_4$:Mn,[51] and LiZn(PO_4):Mn[52], and the orange-red-emitting systems, ZnF_2:Mn,[53] ZnS:Mn,[53] Ba_2ZnS_3,[54] β-$Zn_3(PO_4)_2$:Mn,[55,56] and CaZnGe_2O_6:Mn.[57] In most cases, the manganese doping does not reach 5 mol %. However, other compounds such as $Zn_{2-x}Mn_xP_2O_7 \cdot 5H_2O$ $(0 \le x \le 2.0)$[58] and $Zn_{1-x}Mn_x(O_3PC_6H_5)\cdot H_2O$ $(0 \le x \le 1.0)$[59] can form complete solid solutions between zinc and manganese end members.

In order to explore the possibility of enhancing the luminescence properties of Mn^{2+} in $Mn_2(HPO_3)F_2$, we have partially replaced Mn^{2+} with Zn^{2+} ions and obtained the solid solutions $(Mn_xZn_{1-x})_2(HPO_3)F_2$ with Mn^{2+} concentrations of ~57% (MnZn1), ~34% (MnZn2), and ~22% (MnZn3) relative to that of the stoichiometric compound (100%).

As an example, Figure 9 shows the excitation and emission spectra of the less concentrated sample, MnZn3, with the corresponding energy level assignations. It is worth noticing that the energy absorption bands correspond to a d^5 configuration ion in an octahedral site.

A similar study of the luminescence properties has been performed as a function of Mn^{2+} concentration. Samples MnZn2 and MnZn3 show room temperature luminescence, whereas the emission of sample MnZn1 is practically quenched at 225 K. In the three samples, the emission spectra, measured

dx.doi.org/10.1021/ic201226t | Inorg. Chem. 2011, 50, 12463–12476

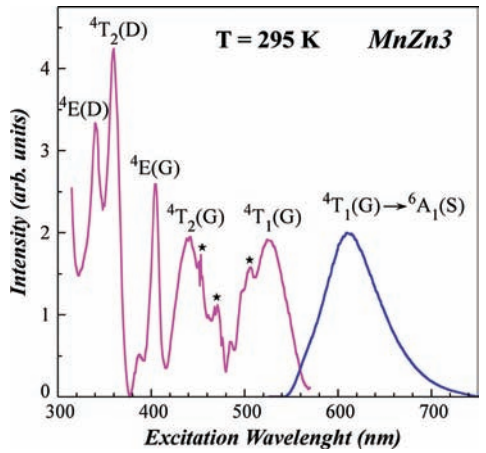

Figure 9. Excitation and emission spectra of the MnZn3 sample. The stars are artifacts due to energy lamp corrections.

under excitation at 514 nm between 77 and 295 K, show a broad band centered at around 629 nm.

As an example, Figure 10 shows the emission spectra as a function of the temperature for the less concentrated sample MnZn3.

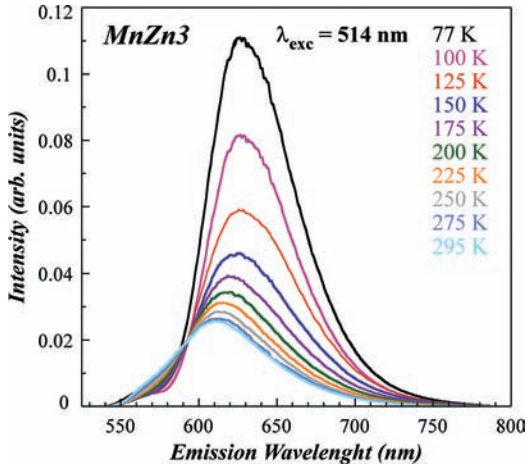

Figure 10. Temperature dependence of the emission spectra of MnZn3.

The full width at half-maximum (fwhm) of the emission peak is about 63 nm at 77 K for the three samples and slightly increases up to 71 nm at 295 K for samples MnZn3 and MnZn2. When the temperature increases from 77 to 295 K, the emission bands of these samples show a global blue shift of about 16 nm. However, in the region between 77 K and about 130 K, samples MnZn1 and MnZn2 show a lightly red shift following the trend of the concentrated $Mn_2(HPO_3)F_2$ phase. The red shift can be attributed to the coupling between adjacent Mn^{2+} ions, which leads to rapid energy transfer among ions and populates Mn^{2+} sites with a lower energy. In fact, the octahedral coordination of the manganese ion displays a variety of bond lengths, R (Mn−F, Mn−O) in which R may change as much as 6% for a given compound. Figure 3 presents a picture of the Mn^{2+} coordination together with the bond lengths for all of the compounds studied. On the other hand, the blue shift of the emission band as the temperature increases depends on the strength $\Delta = 10Dq$ of the crystal field, which in turn is a function of the distance R between the absorbing center and the ligands. $\Delta \propto R^{-5}$ in the charge model, and R is a function of the temperature through the expansion coefficient of the material. $R(T) = R(0)(1 + \alpha T)$ where $\alpha \sim 10^{-5}$ is the linear expansion coefficient. Therefore

$$\Delta \propto \frac{K}{R^n} = \frac{K}{R(0)^n(1+\alpha T)^n} \approx \frac{K}{R(0)^n}(1 - n\alpha T)$$

An expansion of the crystal reduces the crystalline field strength and changes the transition frequency, which therefore depends on the temperature. The law by which the frequency varies depends on the slope $dE/d\Delta$ of the curve of energy versus Δ in the Tanabe−Sugano diagrams. In our case, we have a negative slope for the d^5 ion, and as a consequence, the band shifts to blue. Figure 11 shows the peak position of the emission band as a function of the temperature for the studied samples.

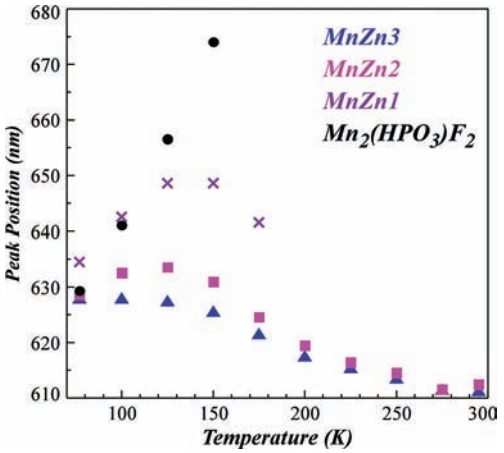

Figure 11. Peak position of the emission band as a function of the temperature.

Figure 12 shows the integrated emission intensity as a function of the temperature for the three samples normalized at 77 K. The values of the concentrated sample were also included for comparison.

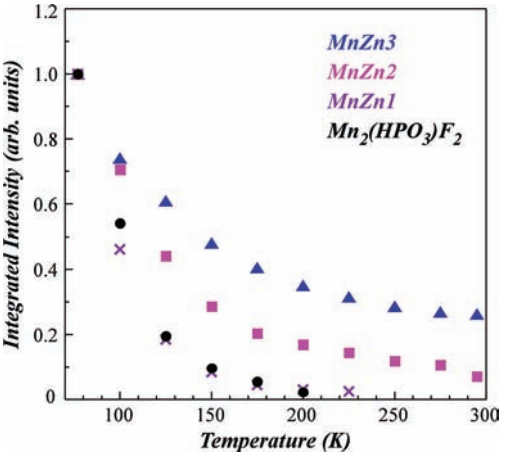

Figure 12. Integrated emission intensity as a function of the temperature for MnZn1, MnZn2, MnZn3, and $Mn_2(HPO_3)F_2$ samples.

dx.doi.org/10.1021/ic201226t | Inorg. Chem. 2011, 50, 12463–12476

As can be observed, sample MnZn1 presents the same thermal quenching behavior as the concentrated sample, whereas, as expected, the most efficient emission is from the lowest concentrated MnZn3 sample, which at 295 K gives an emission intensity of about 26% of the one measured at 77 K.

In various manganese doped host materials, concentration quenching is found to occur around 15 mol %. For instance, in the green-emitting phosphor $BaMgAl_{10}O_{17}:Eu^{2+},Mn^{2+}$[60] the intensity of the emission peak reaches a maximum when the ratio of Mn^{2+} is 13 mol %. In $BaMgP_2O_7:Eu^{2+},Mn^{2+}$,[61] the optimum concentration of Mn^{2+} to reach the red emission maximum is 17.5 mol %. In α-$Ca_2P_2O_7:Eu^{2+},Mn^{2+}$,[62] the strongest intensity of the orange band is achieved with a concentration of Mn^{2+} of 12 mol %, and in $LiZn_{1-x}PO_4:Mn_x$ ($0 < x \leq 0.22$),[63] the yellow-green emission intensity for all excitation wavelengths increased with increasing Mn^{2+} concentration until a maximum intensity was reached at 12 mol %.

In our case, we were able to reduce the Mn content of the $Mn_2(HPO_3)F_2$ compound with the insertion of Zn until reaching around 22 mol % of Mn in the MnZn3 sample. Light efficiency would improve if it were possible to reduce even more the concentration of Mn^{2+}, but up to now the attempts to insert more zinc produced instability in the $Mn_2(HPO_3)F_2$ crystal structure.

The concentration dependence of the decays of the red emission was obtained as a function of the temperature. In this case, the decays were not single exponentials at all temperatures for the three samples. They present an initial nonexponential decay that can be attributed to direct energy transfer among Mn^{2+} ions. This fast component does not appear in the case of the $Mn_2(HPO_3)F_2$ sample due to a fast energy diffusion among Mn^{2+} ions. In this case, variations in the transfer times are effectively averaged out, and the system shows a single exponential decay.[64]

The lifetime values, which correspond to the average lifetime defined by $\langle\tau\rangle = (\int I(t)\ dt)/I_0$, as a function of the temperature, are displayed in Figure 13 for the three samples.

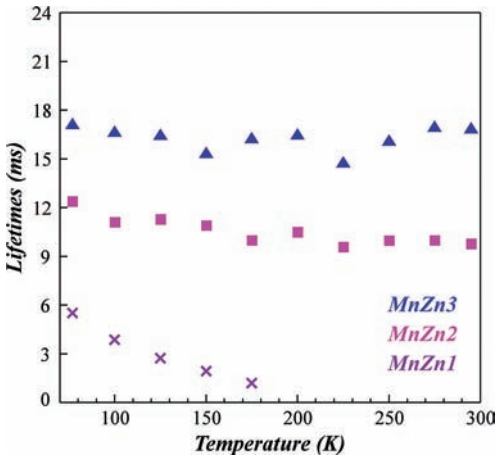

Figure 13. Lifetimes as a function of the temperature.

As can be seen, the lifetimes decrease as the Mn^{2+} concentration increases even at low temperatures, which indicates the presence of efficient energy transfer processes among Mn^{2+} ions. As a matter of fact, due to the long lifetime of the $^4T_1$ state, the excitation in this state will migrate among Mn^{2+} ions and "sample" a large portion of the crystal. This leads to efficient feeding of any traps in the material resulting in concentration quenching.[65]

In spite of the Mn−Zn substitution limitations of the finite solid solution $(Mn_xZn_{1-x})_2(HPO_3)F_2$, the lifetime value of the MnZn3 sample at room temperature is 16.9 ms. This value is much higher than those registered by many hosts, in which the effect of Mn^{2+} concentration on luminescence properties has been studied. For example, lifetime shortening was reported to range from 7.2 to 4.5 ms in $MgAl_2O_4/Mn^{2+}$ (0.2−10 mol %),[66] from 15 to 1.8 ms in Zn_2SiO_4/Mn^{2+} (0.1−5 mol %),[66] and from 11 to 9.5 ms in $NaCaPO_4/Mn^{2+}$ (1−22 mol %).[67]

3.5.d. Diffuse Reflectance Spectrum of $Fe_2(HPO_3)F_2$ (2). In the diffuse reflectance spectrum of **2**, two bands at approximately 9240 and 7190 cm^{-1} are observed. These bands are characteristic of the iron(II) d^6-high spin cation in a slightly distorted octahedral environment and correspond to the electronic transitions from the $^5T_{2g}(^5D)$ fundamental state to the excited level $^5E_{2g}(^5D)$ that is split as a consequence of the existence of nonregular $[FeO_3F_3]$ octahedra. The energy associated with this transition corresponds, according to the Tanabe−Sugano diagram,[68,69] to the Dq parameter. The value obtained is Dq = 820 cm^{-1}. These results are in good agreement with the values observed in other related compounds containing this cation[45] (Figure S12, Supporting Information).

3.6. Magnetic Behavior and Specific Heat Measurements. The magnetic susceptibility of compounds **1** and **2** has been measured on powdered samples from room temperature to 5 K, in the Zero Field Cooling (ZFC) and Field Cooling (FC) modes, at 1000, 500, and 100 Oe (Figure 14).

The molar magnetic susceptibility continuously increases from 300 to 32 K and 36 K, for **1** and **2**, respectively. Below these temperatures, the FC curves show an abrupt increase until approximately 5 K, whereas the ZFC curves increase until 30 K and then decrease. The susceptibility follows the Curie−Weiss law above 50 K for **1** and **2**, with values of the Curie and Curie−Weiss temperature of Cm = 8.93 cm^3 K/mol (**1**) and 7.51 cm^3 K/mol (**2**) and θ = −62.5 K (**1**) and −85.8 K (**2**). In both phases **1** and **2**, the $\chi_m T$ vs T curve decreases with decreasing temperature, showing a maximum at approximately 30 K, from which this curve increases and finally decreases again. These results indicate a global antiferromagnetic behavior with a ferromagnetic component, at approximately 30 K, for both compounds.

The susceptibility measurements carried out at 500 and 100 Oe for both phases show irreversibility when they are performed in the ZFC and FC modes (see Figure 14). This result suggests the existence of weak ferromagnetic components at low temperatures, in good agreement with the abrupt increase of the χ_m and $\chi_m T$ vs T curve observed at approximately 30 K.

In order to corroborate the existence of these ferromagnetic components in the phases, magnetization measurements at different magnetic fields were performed (Figure 15). It was found that, unlike compound **1**, compound **2** exhibits hysteresis loops in which the intensity varies with the temperature (Table 4). At 5 K, the values of the remnant magnetization and coercive field are 0.168 μ_B and 16.35 KOe, respectively. In addition, the remnant magnetization was evaluated by cooling samples in the presence of magnetic fields of 100 Oe for **1** and 70 KOe for **2** and then heating them. These measurements show that magnetization disappears at temperatures of 32 and 36 K for **1** and **2**, respectively. These results confirm the

dx.doi.org/10.1021/ic201226t | Inorg. Chem. 2011, 50, 12463–12476

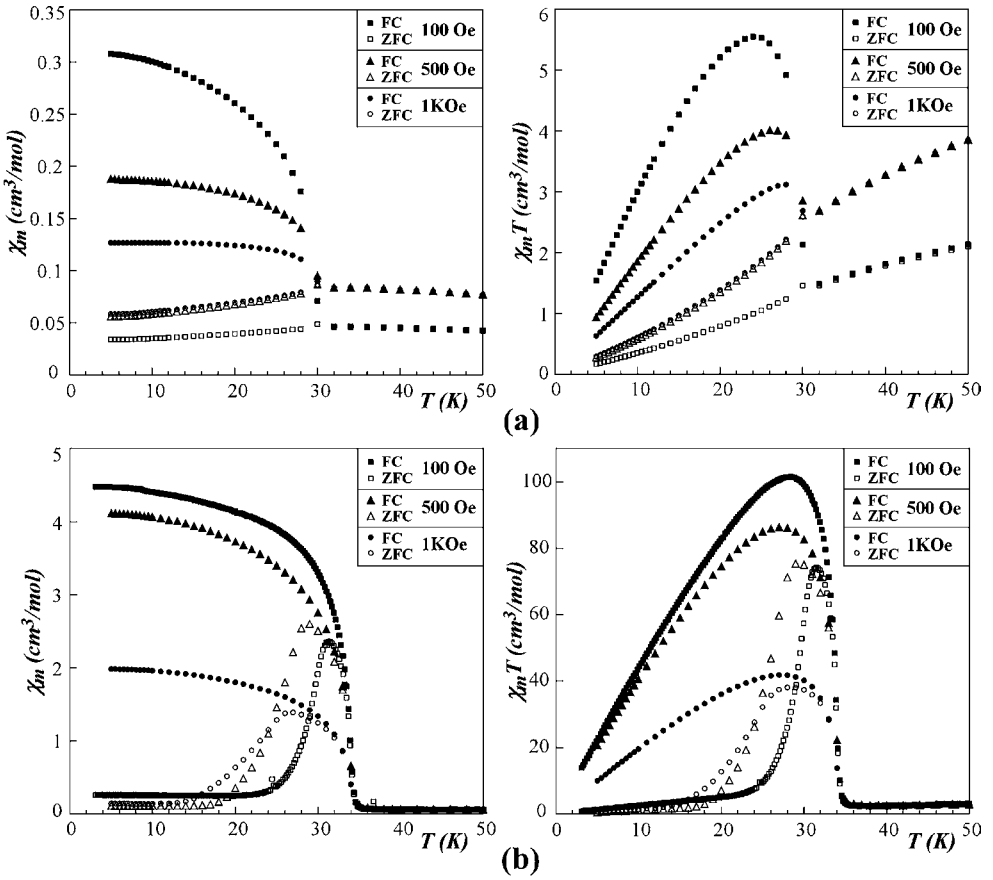

Figure 14. Thermal evolution of the χ_m and $\chi_m T$ curves for (a) $Mn_2(HPO_3)F_2$ (**1**) and (b) $Fe_2(HPO_3)F_2$ (**2**).

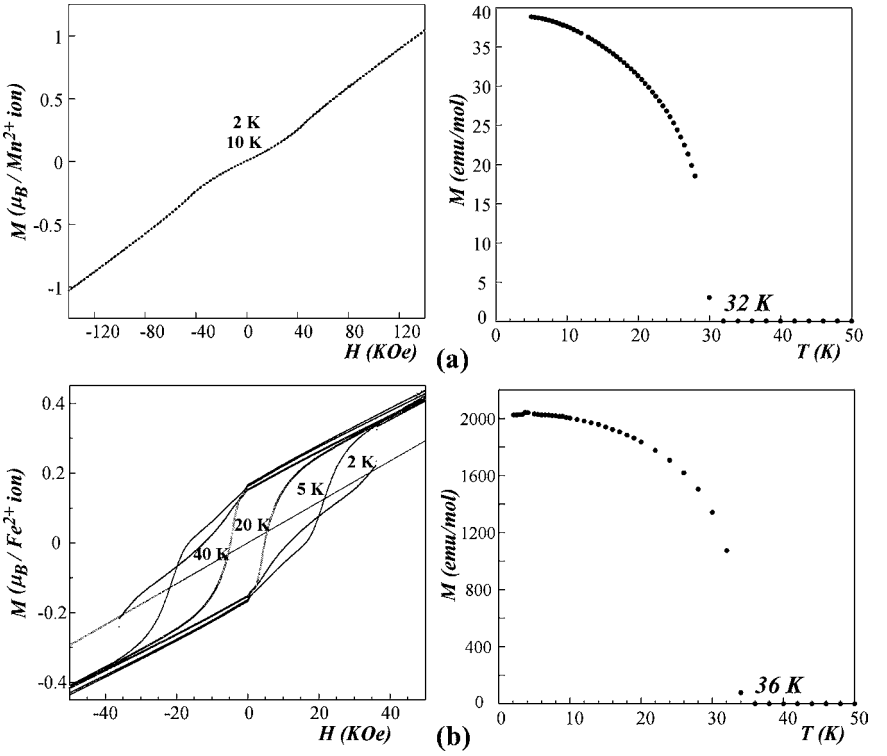

Figure 15. Hysteresis loops and remnant magnetization of (a) $Mn_2(HPO_3)F_2$ (**1**) and (b) $Fe_2(HPO_3)F_2$ (**2**).

existence of weak ferromagnetic components in the two phases, probably due to spin canting phenomena.

The specific-heat data between 2 and 300 K are shown in Figure 16. The heat-capacity measurements exhibit a sharp

dx.doi.org/10.1021/ic201226t | Inorg. Chem. 2011, 50, 12463–12476

Table 4. Remnant Magnetization (emu/mol) and Coercitive Field (KOe) at Different Hysteresis Loop Measurement Temperatures for 2

temperature	remnant magnetization	coercitive field
2 K	0.165 μ_B	11.58 KOe
5 K	0.168 μ_B	16.35 KOe
20 K	0.152 μ_B	4.84 KOe
40 K	does not show hysteresis loop	

magnetic peak at 29.7 and 33.5 K, for the manganese(II) and iron(II) compounds, respectively. The temperatures at which these peaks appear are similar to those obtained from the magnetic susceptibility measurements.

The strong increase of Cp at higher temperatures is due to the lattice contribution (Cp_{pho}). In order to determine Cp_{pho}, we fitted the experimental data above the magnetic transition to the Debye model; however, a large difference between both the theoretical and experimental data was observed. The reason for such a discrepancy can be attributed to the presence in the unit cell of atoms such as Fe, Mn, and P with higher masses than those of the O and H atoms. Therefore, more than one phonon spectrum can be present in every compound. For this reason, we determine Cp_{pho} using a Debye model with two Debye temperatures (minimum number of free parameters which allow us to fit the experimental data). In this way, if the number of atoms in the unit cell is N, we suppose n_1 atoms with a Debye temperature θ_1 and n_2 atoms $[n_2 = (N - n_1)]$ with a Debye temperature θ_2. Therefore, there are three free parameters, namely, n_1, θ_1, and θ_2. The best fitting is obtained for $n_1 = 5.05$ and $\theta_1 = 349.22$ K and for $n_2 = 3.95$ and $\theta_2 = 1120.07$ K in the case of the manganese(II) phase and $n_1 = 4.87$ and $\theta_1 = 348.6$ K and $n_2 = 4.13$ and $\theta_2 = 1165.4$ K in the case of the iron(II) one. The good quality of the fits (see the continuous line in Figure 16) allows us to consider that this phenomenological model reasonably well determines the phonon contribution. The magnetic contribution was calculated as $Cp_{mag} = Cp - Cp_{pho}$ and has a Gaussian shape, extending up to approximately 50 K in both compounds, see inset in Figure 16.

The effect of the magnetic fields on Cp has also been studied. With increasing field, the maximum becomes more rounded and shifts to lower temperatures, for both phases. This effect is clearly observed in the magnetic contribution, see Figure 17, where the maximum shifts from 29.7 to 29.1 K and from 33.5 to 32.6 K for the Mn(II) and Fe(II) phases, respectively, when the field increases from 0 to 9 T. These results are in good agreement with global antiferromagnetic behaviors for both compounds, as was also observed from the magnetic susceptibilities.

The total magnetic entropy for the Mn(II) phase was found to be 3.7R, which agrees with the theoretical value (3.58R) for an $S = 5/2$ (see Figure S13, Supporting Information). An amount of 81% (2.98R) was gained below the ordering temperature. The rest of entropy could be attributed to the short-range interactions. For the Fe(II) compound, the total magnetic entropy was 2.7R, which is nearer to an $S = 2$ system (theoretical value 3.22R) than to an $S = 5/2$ system (theoretical value 3.58R). Similarly to the manganese(II) phase, approximately 76% (2.04R) of the entropy of the iron(II) compound is gained below the ordering temperature.

4. CONCLUDING REMARKS

The mild hydrothermal technique has been used for the synthesis of $Mn_2(HPO_3)F_2$ (**1**) and the different finite solid solutions (MnZn1, MnZn2, and MnZn3) of $(Mn_xZn_{1-x})_2(HPO_3)F_2$ formula. The crystal structure of these phases consists of a three-dimensional network formed by alternating (010) layers of $[(Mn,Zn)O_3F_3]$ octahedra linked up by three-connected $[HPO_3]$ tetrahedra.

The luminescent properties of the octahedrally coordinated Mn^{2+} cations in these phases show a red emission peaking between 615 and 630 nm associated with the $^4T_1 \rightarrow {}^6A_1$ transition. $(Mn_xZn_{1-x})_2(HPO_3)F_2$ system shows that the progressive insertion of Zn^{2+} in the Mn^{2+} site maintaining the crystal structure of the stoichiometric compound (**1**) reduces the temperature concentration quenching. So, due to the partial elimination of the nonradiative processes caused by the dilution of the manganese pure compound, less manganese concentrated samples, such as MnZn2 and MnZn3, show room temperature luminescence, the latter being the most efficient one, giving at 295 K an emission intensity of about 26% of the one measured at 77 K. In spite of the Mn−Zn substitution limitations of the $(Mn_xZn_{1-x})_2(HPO_3)F_2$ system, the lifetime value of the less manganese concentrated sample, MnZn3 (∼ 22% Mn), is as high as 17 ms.

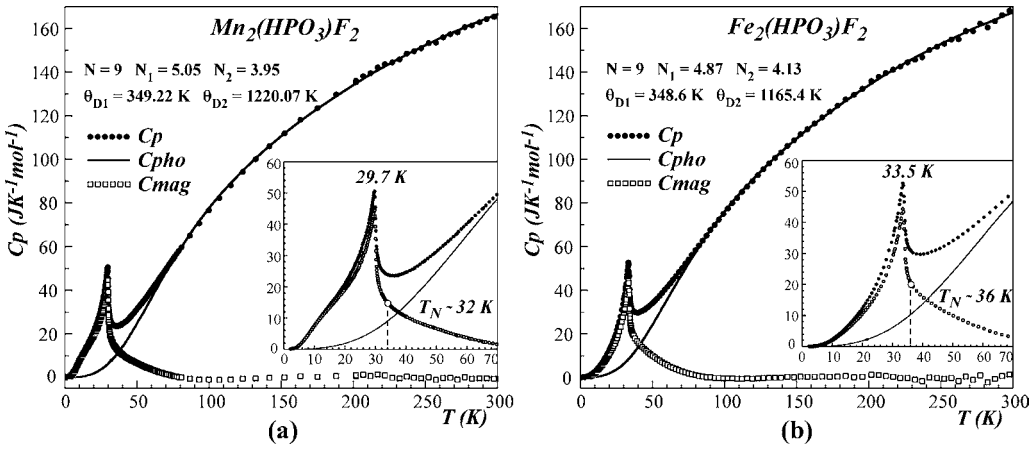

Figure 16. Thermal evolution of Cp, Cphon, and Cmag of (a) $Mn_2(HPO_3)F_2$ (**1**) and (b) $Fe_2(HPO_3)F_2$ (**2**).

dx.doi.org/10.1021/ic201226t | Inorg. Chem. 2011, 50, 12463–12476

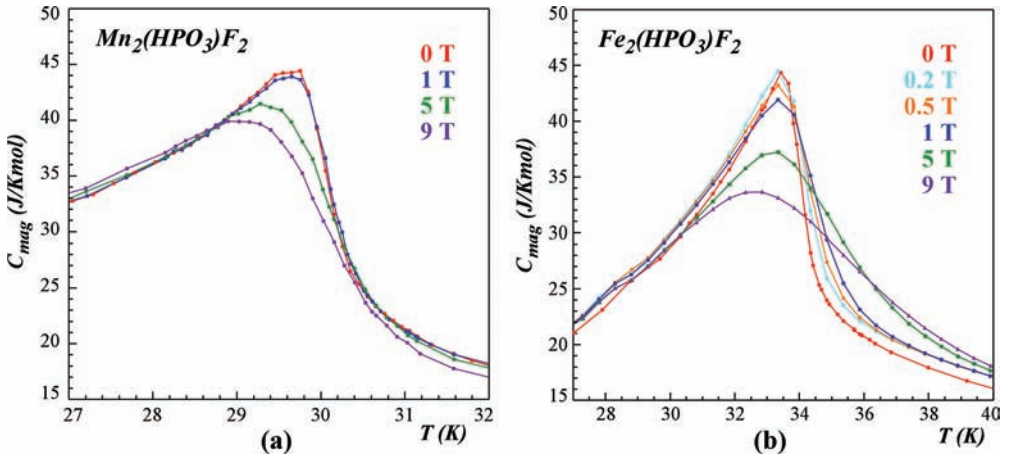

Figure 17. Specific-heat magnetic data under different magnetic fields for (a) $Mn_2(HPO_3)F_2$ (**1**) and (b) $Fe_2(HPO_3)F_2$ (**2**).

Magnetization measurements of $Mn_2(HPO_3)F_2$ (**1**) and the isostructural compound $Fe_2(HPO_3)F_2$ (**2**) are consistent with the existence of major antiferromagnetic interactions and weak ferromagnetism due to a spin canting phenomenon detected at approximately 30 K. In the specific heat measurements, a λ-type peak consistent with the 3D magnetic ordering of both phases is observed. The total magnetic entropy is typical of Mn(II) and Fe(II) cations.

■ ASSOCIATED CONTENT

Ⓢ Supporting Information

(Figure S1) Polycrystalline powder of the $Mn_2(HPO_3)F_2$ phase (**1**) and single crystals of the same phase obtained as a result of the addition of $CeCl_3{\cdot}7H_2O$ to the synthesis. (Figure S2) View of the relation of the structural subunits of the $Mn_2(HPO_3)F_2$ compound to the several symmetry elements characteristic of the *Pnma* space group, projected along the [100] direction. (Figure S3) Variation of (a) the unit cell parameters and (b) the M−O and M−F (M = Mn, Zn) distances as a function of the occupation factors of the manganese atoms for $Mn_2(HPO_3)F_2$ (**1**) and for the main solid solutions present in the MnZn1, MnZn2, and MnZn3 samples. (Figure S4) Distortion values of the $[(Mn,Zn)O_3F_3]$ octahedra and $[HPO_3]$ tetrahedra belonging to $Mn_2(HPO_3)F_2$ (**1**) and to the different members of the finite solid solution of the MnZn1, MnZn2, and MnZn3 samples. (Figure S5) Observed, calculated, and difference X-ray powder diffraction patterns for $Fe_2(HPO_3)F_2$ (**2**) with the structural model of $Mn_2(HPO_3)F_2$ (**1**). (Figure S6) Thermal analysis (TGA, DTA) of $Mn_2(HPO_3)F_2$ (**1**) and $Fe_2(HPO_3)F_2$ (**2**). (Figure S7) Thermodiffractograms of (a) $Mn_2(HPO_3)F_2$ (**1**) and (b) the MnZn3 sample. (Figure S8) Thermodiffractogram of $Fe_2(HPO_3)F_2$ (**2**). (Figure S9) Thermal evolution of the parameters and volume of the unit cells for $Mn_2(HPO_3)F_2$ (**1**) and $Fe_2(HPO_3)F_2$ (**2**) in the 30−435 °C temperature range. (Figure S10) Infrared spectra of compounds **1** and **2**. (Figure S11) Wavelength shift of the bands corresponding to the stretching vibrational mode, ν(P−H), of the phosphite groups of $Mn_2(HPO_3)F_2$ (**1**) and the MnZn1, MnZn2, and MnZn3 samples. (Figure S12) Diffuse reflectance spectrum of $Fe_2(HPO_3)F_2$ (**2**). (Figure S13) Magnetic entropy of (a) $Mn_2(HPO_3)F_2$ (**1**) and (b) $Fe_2(HPO_3)F_2$ (**2**) as a function of the temperature. The horizontal lines show the theoretical values expected for the entropy of each system, s = 5/2 for **1** and s = 2 for **2**.

See Tables S1−S12 for atomic coordinates, B_{iso}(Å^2), and bond distances and angles of the Rietveld refinements of all of the phases present in the MnZn1, MnZn2, and MnZn3 samples. (Table S13) Distortion values for $[M(1)O_3F_3]$ (M = Mn, Zn) and $[HP(1)O_3]$ coordination polyhedra for **1** and the phases present in the MnZn1, MnZn2, and MnZn3 samples. (Table S14) Crystallographic parameters and characteristics of the Rietveld refinement for **2**. (Table S15) Atomic coordinates and B_{iso}(Å^2) for **2**. (Table S16) Bond distances (Å) and angles (deg) for **2**. (Table S17) Thermal expansion coefficients of the parameters and volume of the unit cells for **1** and **2**. (Table S18) Assignment of the infrared spectra bands of the compounds **1** and **2**. Crystallographic information files (CIF). This information is available free of charge via Internet at http://pubs.acs.org/.

■ AUTHOR INFORMATION

Corresponding Author

*Phone: 34-946012162. Fax: 34-946013500. E-mail: maribel.arriortua@ehu.es.

■ ACKNOWLEDGMENTS

This work has been financially supported by the "Ministerio de Educación y Ciencia" (MAT2010-15375) and the "Gobierno Vasco" (IT-177-07 and IT-331-07), which we gratefully acknowledge. The authors thank the technicians of SGIker (UPV/EHU), Drs. I. Orue, F.J. Sangüesa, P. Vitoria, and A. Larrañaga, financed by the National Program for the Promotion of Human Resources within the National Plan of Scientific Research, Development and Innovation, "Ministerio de Ciencia y Tecnologí;a" and "Fondo Social Europeo" (FSE), for the magnetic measurements and the X-ray diffraction measurement, respectively. J.O. wishes to thank the "Departamento de Educación, Universidades e Investigación del Gobierno Vasco/Eusko Jaurlaritza" and the Universidad del País Vasco/EHU for funding.

■ REFERENCES

(1) Schubert, E. F.; Kim, J. K. *Science* **2005**, *308*, 1274.
(2) Höppe, H. A. *Angew. Chem., Int. Ed.* **2009**, *48*, 3572.
(3) Guo, C.; Gao, F.; Xu, Y.; Liang, L.; Shi, F. G.; Yan, B. *J. Phys. D: Appl. Phys.* **2009**, *42*, 095407.
(4) Ren, F.; Chen, D. *Opt. Laser Technol.* **2010**, *42*, 110.
(5) Tang, Y.-S.; Hu, S.-F.; Lin, C. C.; Bagkar, N. C.; Liu, R.-S. *Appl. Phys. Lett.* **2007**, *90*, 151108.

(6) Kwon, K. H.; Im, W. B.; Jang, H. S.; Yoo, H. S.; Jeon, D. Y. *Inorg. Chem.* **2009**, *48*, 11525.
(7) Blasse, G. *J. Solid State Chem.* **1975**, *14*, 181.
(8) Pappalardo, R. G.; Walsh, J.; Hunt, R. *J. Electrochem. Soc.* **1983**, *130*, 2087.
(9) Kottaisamy, M.; Jagannathan, R.; Jeyagopal, P.; Rao, R. P.; Narayanan, R. L. *J. Phys. D: Appl. Phys.* **1994**, *27*, 2210.
(10) Gaft, M.; Panczer, G.; Reisfeld, R.; Uspensky, E. *Phys. Chem. Miner.* **2001**, *28*, 347.
(11) Yang, P.; Yao, G.-Q.; Lin, J.-H. *Inorg. Chem. Commun.* **2004**, *7*, 302.
(12) Sahoo, R.; Bhattacharya, S. K.; Debnath, R. *J. Solid State Chem.* **2003**, *175*, 218.
(13) Zeng, Q.; Liang, H.; Zhang, G.; Birowosuto, M. D.; Tian, Z.; Lin, H.; Fu, Y.; Dorenbos, P.; Su, Q. *J. Phys.: Condens. Matter* **2006**, *18*, 9549.
(14) Zhang, C.; Huang, S.; Yang, D.; Kang, X.; Shang, M.; Peng, C.; Lin, J. *J. Mater. Chem.* **2010**, *20*, 6674.
(15) Im, W. B.; Fourr, Y.; Brinkley, S.; Sonoda, J.; Nakamura, S.; DenBaars, S. P.; Seshadri, R. *Opt. Express* **2009**, *17*, 22673.
(16) Im, W. B.; Brinkley, S.; Hu, J.; Mikhailovsky, A.; DenBaars, S. P.; Seshadri, R. *Chem. Mater.* **2010**, *22*, 2482.
(17) Fang, Y.; Li, Y. Q.; Qiu, T.; Delsing, A. C. A.; de With, G.; Hintzen, H. T. *J. Alloys Compd.* **2010**, *496*, 614.
(18) Chen, W.; Liang, H.; Ni, H.; He, P.; Su, Q. *J. Electrochem. Soc.* **2010**, *157*, J159.
(19) Setlur, A. A.; Radkov, E. V.; Henderson, C. S.; Alok, J-H. H.; Srivastava, M.; Karkada, N.; Kishore, M. S.; Kumar, N. P.; Aesram, D.; Deshpande, A.; Kolodin, B.; Grigorov, L. S.; Happek, U. *Chem. Mater.* **2010**, *22*, 4076.
(20) Rojo, T.; Mesa, J. L.; Lago, J.; Bazán, B.; Pizarro, J. L.; Arriortua, M. I. *J. Mater. Chem.* **2009**, *19*, 3793.
(21) Chung, U.-C.; Mesa, J. L.; Pizarro, J. L.; Jubera, V.; Lezama, L.; Arriortua, M. I.; Rojo, T. *J. Solid State Chem.* **2005**, *178*, 2913.
(22) Orive, J.; Mesa, J. L.; Legarra, E.; Plazaola, F.; Arriortua, M. I.; Rojo, T. *J. Solid State Chem.* **2009**, *182*, 2191.
(23) Guth, J. L.; Kessler, H.; Wey, R. *Stud. Surf. Catal.* **1986**, *28*, 121.
(24) Sugano, S.; Tanabe, Y. *Multiplets of Transition-Metal Ions in Crystals*; Academic Press: New York, 1970.
(25) Yen, W. M.; Shionoya, S.; Yamanoto, H. *Phosphor Handbook*; CRC Press: Boca Raton, FL, 2007.
(26) Liu, L.; Wang, X.; Xu, L.; Liu, X.; Liu, L.; Bi, B.; Pang, W. *Inorg. Chim. Acta* **2009**, *362*, 3881.
(27) Feng, S.; Xu, R. *Acc. Chem. Res.* **2001**, *34*, 239.
(28) Sheldrick, G. M. *SHELXS 97*; University of Göttingen: Göttingen, Germany, 1977.
(29) Sheldrick, G. M. *SHELXL 97*; University of Göttingen: Göttingen, Germany, 1977.
(30) Dowty, E. *ATOMS*; Shape Software: Kingsport, TN, 1993.
(31) Rodriguez-Carvajal, J. *Phys. B* **1993**, *192*, 55.
(32) Álvarez, S.; Avnir, D.; Llunel, M.; Pinsky, M. *New. J. Chem.* **2002**, *26*, 996.
(33) Llunel, M.; Casanova, D.; Cirera, J.; Bofill, J. M.; Alemany, P.; Alvarez, S.; Pinski, M.; Yatumir, D. *SHAPE v1.1a*; Universitat de Barcelona: Barcelona, Spain, 2003.
(34) Cirera, J.; Alemany, P.; Álvarez, S. *Chem.—Eur. J.* **2004**, *10*, 190.
(35) West, A. R. *Basic Solid State Chemistry*; Wiley: Chichester, West Sussex, U. K., 1988.
(36) Vartanov, A. *Russ. J. Inorg. Chem. (Engl. Transl.)* **1978**, *23*, 341 (PDF no. 33−901).
(37) Arnold, H. *Z. Crystallogr.* **1986**, *177*, 139 (PDF no. 29−715).
(38) Modaressi, A.; Courtois, A.; Gerardin, R.; Malaman, B.; Gleitzer, C. *J. Solid State Chem.* **1983**, *47*, 245 (PDF no. 36−61).
(39) Maslen, E. N.; Strel'tsov, V. A.; Strel'tsova, N. R.; Ishizawa, N. *Acta Crystallogr. B* **1994**, *50*, 435.
(40) Zachariasen, W. H. *Skr. Nor. Vidensk.-Akad., Kl. 1: Mat.-Naturvidensk. Kl.* **1928**, *1928*, 1 (PDF no. 1−76−150).
(41) Sasaki, S.; Fujino, K.; Takeuchi, Y.; *Acta Crystallogr. A* **1980**, *36*, 904 (PDF no. 7−230).
(42) *Natl. Bur. Stand. (U.S.) Monogr. 25* **1979**, *16*, 83.
(43) Fei, Y. In *AGU Reference Shelf 2: Mineral Physics and Crystallography—A Handbook of Physical Constants*; Ahrens, T. J., Ed.; AGU, Washington, DC, 1995; pp 29−44.
(44) Tsuboi, M. *J. Am. Chem. Soc.* **1957**, *79*, 1351.
(45) Lever, A. B. P. *Inorganic Electronic Spectroscopy*; Elsevier Science Publishers B.V.: Amsterdam, Netherlands, 1984.
(46) Griffith, G. S. *Theory of Transition-Metal Ions*; Cambridge University Press: Cambridge, 1964.
(47) Di Bartolo, B. *Optical Interactions in Solids*; Wiley: New York, 1968.
(48) Xie, R.-J.; Hirosaki, N.; Kimura, N.; Sakuma, K.; Mitomo, M. *Appl. Phys. Lett.* **2007**, *90*, 191101.
(49) Barthou, C.; Benoit, J.; Benalloul, P.; Morell, A. *J. Electrochem. Soc.* **1994**, *141* (2), 524.
(50) Palumbo, D. T.; Brown, J. J. Jr. *J. Electrochem. Soc.* **1970**, *117* (9), 1184.
(51) Poort, S. H. M.; Cetin, D.; Meijerink, A.; Blasse, G. *J. Electrochem. Soc.* **1997**, *144* (6), 2179.
(52) Chan, T.-S.; Liu, R.-S.; Baginskiy, I. *Chem. Mater.* **2008**, *20*, 1215.
(53) Palumbo, D. T.; Brown, J. J. Jr. *J. Electrochem. Soc.* **1971**, *118* (7), 1159.
(54) Thiyagarajan, P.; Kottaisamy, M.; Ramachandra Rao, M. S. *J. Phys. D: Appl. Phys.* **2006**, *39*, 2701.
(55) Song, Y.-H.; Zou, H.-F.; Gan, S.-C.; Deng, Y.-F.; Hong, G.-Y.; Meng, J. *J. Mater. Sci.* **2007**, *42*, 4899.
(56) Wang, J.; Wang, S.; Su, Q. *J. Solid State Chem.* **2004**, *177*, 895.
(57) Che, G.; Liu, C.; Li, X.; Xu, Z.; Liu, Y.; Wang, H. *J. Phys. Chem. Solids* **2008**, *69*, 2091.
(58) Gaïdideï, G. I.; Gomenyuk, O. V.; Nedelko, S. G.; Sleptsov, A. A.; Antraptseva, N. M.; Boïko, V. V.; Tkachova, N. V. *Phys. Solid State* **2005**, *47* (8), 1544.
(59) Singleton, R.; Bye, J.; Dyson, J.; Baker, G.; Ranson, R. M.; Hix, G. B. *Dalton Trans.* **2010**, *39*, 6024.
(60) Yang, P.; Yao, G.-Q.; Lin, J.-H. *Opt. Mater.* **2004**, *26*, 327.
(61) Kim, Y.-K.; Choi, S.; Jung, H.-K. *J. Lumin.* **2010**, *130*, 60.
(62) Hao, Z.; Zhang, J.; Zhang, X.; Sun, X.; Luo, Y.; Lu, S.; Wang, X.-j. *Appl. Phys. Lett.* **2007**, *90*, 261113.
(63) Chan, T.-S.; Liu, R.-S.; Baginskiy, I. *Chem. Mater.* **2008**, *20*, 1215.
(64) Weber, M. J. *Phys. Rev. B* **1971**, *4*, 2932.
(65) Yen, W. M.; Selzer, P. M. *Laser Spectroscopy of Solids*; Springer-Verlag: Berlin, 1981.
(66) Vink, A. P.; de Bruin, M. A.; Roke, S.; Peijzel, P. S.; Meijerink, A. *J. Electrochem. Soc.* **2001**, *148*, E313.
(67) Shi, L.; Huang, Y.; Seo, H. J. *J. Phys. Chem. A* **2010**, *114*, 6927.
(68) Tanabe, Y.; Sugano, S. *J. Phys. Soc. Jpn.* **1954**, *9*, 753.
(69) Orgel, L. E. *J. Chem. Phys.* **1955**, *23*, 1004.